J. Fluid Mech. (2010), *vol.* 647, *pp.* 361–390. © Cambridge University Press 2010
doi:10.1017/S002211200999382X

Tear film dynamics on an eye-shaped domain. Part 2. Flux boundary conditions

K. L. MAKI[1], R. J. BRAUN[1]†, P. UCCIFERRO[1],
W. D. HENSHAW[2] AND P. E. KING-SMITH[3]

[1]Department of Mathematical Sciences, University of Delaware, Newark, DE 19711, USA
[2]Lawrence Livermore National Laboratory, Box 808, L-550, Livermore, CA 94551-0808, USA
[3]College of Optometry, The Ohio State University, Columbus, OH 43218, USA

(Received 6 August 2009; revised 1 December 2009; accepted 3 December 2009)

We model the dynamics of the human tear film during relaxation (after a blink) using lubrication theory and explore the effects of viscosity, surface tension, gravity and boundary conditions that specify the flux of tear fluid into or out of the domain. The governing nonlinear partial differential equation is solved on an overset grid by a method of lines using finite differences in space and an adaptive second-order backward difference formula solver in time. Our simulations in a two-dimensional domain are computed in the OVERTURE computational framework. The flow around the boundary is sensitive to both our choice of flux boundary condition and the presence of gravity. The simulations recover features seen in one-dimensional simulations and capture some experimental observations of tear film dynamics around the lid margins. In some instances, the influx from the lacrimal gland splits with some fluid going along the upper lid towards the nasal canthus and some travelling around the temporal canthus and then along the lower lid. Tear supply can also push through some parts of the black line near the eyelid margins.

1. Introduction

The tear film plays an essential role in the quality of vision and the health of the eye; when functioning properly, it maintains a critical balance between tear secretion and loss with each blink. A collection of problems associated with the malfunction or deficiency of tear film is recognized to be the dry eye syndrome (Lemp 2007). Symptoms of dry eye include blurred vision, burning, foreign body sensation and tearing. Schein *et al.* (1997) estimate that 10–15 % of Americans over the age of 65 have one or more symptoms of dry eye syndrome. Furthermore, Miljanović *et al.* (2007) found dry eye to negatively impact daily tasks such as reading and driving. Thus, a better understanding of the tear film in either healthy or dry eyes could potentially benefit many people (Johnson & Murphy 2004).

The classical description of the tear film is as a thin three-layer film consisting of an anterior oily lipid layer, a middle aqueous layer commonly thought of as tears and a mucus layer. The function of the lipid layer is to decrease the surface tension and retard evaporation. The mucus is secreted from goblet cells and is the first material above the epithelial cells. The classical description of the tear film is not accepted

---

† Email address for correspondence: braun@math.udel.edu

by all and is still debated today. The modern alternate description of the tear film structure does not have the mucus layer as distinct and separate (Bron *et al.* 2004; Gipson 2004), and it is difficult to experimentally measure an interface between the mucus and aqueous layer (King-Smith *et al.* 2004).

The exposed or visible tear film resides on the anterior surface of the eye between the upper and lower lids. We refer to the corners of the eye as either the nasal canthus (near the nose) or the temporal canthus. The tear film thickness distribution has particular characteristics including tear menisci located near the lid margins where the tear film thickness increases at the upper and lower lids. Mishima *et al.* (1966) estimate that 73 % of the exposed tear film volume is located in the upper and lower menisci. Oft-measured parameters associated with the tear menisci are the tear meniscus width (TMW), the thickness of the tear film at the eyelid boundary (i.e. in the direction normal to the eye surface); the tear meniscus height (TMH), the extent of the tear meniscus along the eye surface; and the tear meniscus radius (TMR; sometimes called tear meniscus curvature). In the middle of the cornea, the tear film thickness is much thinner than the TMW. Non-invasive experimental measurements by King-Smith *et al.* (2000) found a tear film thickness of 2.7 μm and, similarly, Wang *et al.* (2003) reported a thickness of 3.3 μm. Moreover, King-Smith *et al.* (2004) found estimates of 3 μm to be consistent with the available evidence.

There have been numerous theoretical studies of Newtonian tear film relaxation on a stationary domain (Wong, Fatt & Radke 1996; Sharma *et al.* 1998; Braun & Fitt 2003). The stationary domain has always been a single line running from the upper lid to the lower lid along the centre of the cornea. The behaviour of the aqueous layer is considered in the presence of the surface tension, viscous effects, gravity and evaporation as well as boundary conditions imposed by the mucus and the lipid layer. In particular, Wong *et al.* (1996) posited a constant curvature meniscus and developed a coating model that relates the initial deposited film thickness to the tear viscosity, surface tension, meniscus radius and upper lid velocity. Creech *et al.* (1998) used the formula yielded from the coating model of Wong *et al.* (1996) to compute tear film thicknesses from experimental lower meniscus curvature measurements. We note that measurements of the cross-sectional radius of curvature in the lower meniscus taken after a blink by Johnson & Murphy (2006) were found to increase with time and vary in space. Tear film relaxation and breakup for a power-law fluid in one space dimension was studied by Gorla & Gorla (2004).

One-dimensional studies with a moving end representing the upper lid have appeared in recent years. The formation of the tear film was first treated theoretically by Wong *et al.* (1996). More recently, Jones *et al.* (2005) gave a unified treatment of the formation and subsequent relaxation of the tear film in single equation models in the limits of a strong surfactant or no surfactant. They demonstrated that the flow from underneath the upper lid was needed to generate a sufficiently uniform tear film to cover the cornea in their models, as was suggested by the analysis of King-Smith *et al.* (2004). Jones *et al.* (2006) studied the formation and relaxation of the tear film in a model with a mobile film surface and insoluble surfactant transport. Among other findings, they were able to quantitatively match experimentally observed speed of upward drift in the tear film following a blink (Berger & Corrsin 1974; Owens & Phillips 2001). Braun & King-Smith (2007) and Heryudono *et al.* (2007) computed solutions for complete blink cycles, including the closing phase, for models using sinusoidal and realistic lid motion, respectively. In both cases, they made quantitative comparison with *in vivo* measurements of tear film thickness following a partial blink; good agreement was found between theory and experiment by Heryudono *et al.* (2007). Tear film formation and relaxation with reflex tearing was treated by Maki *et al.* (2008), and comparison with *in vivo* measurements at the centre of the cornea were favourable. Tear film formation and relaxation was studied in a model with an Ellis fluid approximating the tear film and a tangential-stress-free film surface by Jossic *et al.* (2009).

To our knowledge, the first computations of flow in the tear film in a stationary two-dimensional eye-shaped domain were carried out by Maki *et al.* (2010). They solved a lubrication model for a Newtonian fluid on an eye-shaped domain obtained from a digital photo of an eye subject to specified film thickness and pressure around the boundary. This model explored the consequences of specifying the film curvature (proportional to pressure) as in Wong *et al.* (1996). Maki *et al.* (2010) found that if the boundary pressure was 'frozen' for all time in the simulation, then a strong pressure difference was preserved throughout the computation, leading to a steepening of the pressure field inside the film as time increased. The resulting two-dimensional structure is a generalization of observed steepening in one dimension found by Bertozzi *et al.* (1994) as well as in tear film models (e.g. Braun & Fitt 2003). This kind of pressure boundary condition also preserved strong low-pressure regions in the canthi (the 'corners' of the eye), which enhanced the tendency of the canthi to draw fluid into the large curvature area. If the pressure is relaxed to a constant value around the boundary, then the flow along the boundary was rapidly reduced by comparison. In either case, there is flow out of the domain along the boundary when specifying a pressure boundary condition together with an increased boundary thickness corresponding to the meniscus. The results were sensitive to gravity due to the amount of fluid in the menisci and canthi, but the gravitationally influenced dynamics took longer to develop than a typical interblink period.

In this paper, we specify the amount of tear fluid entering and leaving the domain via the normal component of the flux rather than specifying the pressure. Flux boundary conditions are in some ways a more natural choice for studying tear film dynamics. Theory and measurements for the drainage of tear fluid out the puncta and through the canaliculi are available (e.g. Zhu & Chauhan 2005 and references therein). For the influx of tear fluid from the lacrimal gland, some estimates have appeared in the literature as well (Mishima *et al.* 1966). We believe that using this boundary data is a step closer to realistic modelling of tear film dynamics. We use an extension of the relaxation model of Braun & Fitt (2003) and other workers to a stationary two-dimensional domain in order to explore the consequences of specifying (i) the tear flux at the boundary, (ii) the eye-shaped geometry and (iii) gravitational effects on the tear film thickness and tear fluid flow.

We are interested in understanding the flow of tear fluid between the upper and lower menisci. Maurice (1973) describes the motion of lamp black in the menisci. Just after a blink, the particles in the upper meniscus near the temporal canthus diverged with some particles moving along the upper lid and some around the temporal canthus and along the lower lid. In both cases, the particles travelled towards the nasal canthus. More recently, Harrison *et al.* (2008) visualized the flow of the tear fluid *in vivo*. In their experiments, a solution of fluorescein was introduced under the temporal upper lid close to the temporal canthus; the lid was released and the fluorescein was monitored. Within 3 s, a portion of fluorescein had moved rapidly around the lower meniscus towards the nasal canthus. The remaining fluorescein moved slowly in the upper meniscus towards the nasal canthus. After 35 s, the fluorescein had only travelled over two-thirds of the upper meniscus. The tear flow from the upper meniscus to the lower meniscus through the temporal canthus is referred to here as hydraulic connectivity. We shall see that in some cases our model captures splitting of the flow in the upper meniscus and hydraulic connectivity.

Our evolution equation is solved numerically with an overset grid method on an eye-shaped domain constructed from measured eyelid data. A number of successful methods have been employed for thin film problems, including fully discrete methods, finite differences (FD) in both space and time (e.g. Wong, Fatt & Radke 1996; Oron & Bankoff 2001), FD methods in space with ordinary differential equation (ODE) solvers in time (e.g. Braun & Fitt 2003; Braun & King-Smith 2007), spectral methods with ODE solvers in time (e.g. Heryudono *et al.* 2007), FD in space with alternating direction implicit (ADI) (e.g. Schwartz *et al.* 2001; Witelski & Bowen 2003; Greer, Bertozzi & Sapiro 2006), adaptive FD methods (e.g. Bertozzi *et al.* 1994; Lee, Thompson & Gaskell 2007), positivity preserving schemes (e.g. Grün & Rumpf 2000; Zhornitskaya & Bertozzi 2000; Kondic & Diez 2001), finite element methods (e.g. Grün & Rumpf 2000; Becker *et al.* 2002; Becker & Grün 2005) and publicly available parabolic partial differential equation (PDE) solvers (e.g. Warner, Craster & Matar 2002). Perhaps the closest to our needs of all of these methods is Greer *et al.* (2006), which has general capability in stationary geometry. Given the challenges of the eye-shaped geometry, i.e. the curved boundaries and canthi, we have chosen to discretize the domain with overlapping grids: curvilinear boundary-fitted grids resolve boundary regions and an underlying Cartesian grid approximates the solution away from the boundaries. This overset grid method was used in our previous work with pressure boundary conditions (Maki *et al.* 2010). An overlapping grid approach also has the capability to manage time-dependent overlapping grids, and using this method to compute the case of a blinking eye-shaped domain is a major goal of this ongoing project. The OVERTURE computational framework has built-in capabilities to handle the complex moving domain efficiently, and therefore using this approach here moves us closer to our goal.

We begin by formulating the problem in § 2. The details of the overset grid method are explained in § 3. Finally, in § 4, we explore the effects of the eye-shaped geometry, gravity, as well as different flux boundary conditions on the tear film dynamics. Discussion and conclusions are given in § 5.

2. Formulation

Our model is an extension of the tear film relaxation model in one spatial dimension developed by Braun & Fitt (2003). The tear film is assumed to be a thin film on a two-dimensional eye-shaped geometry, shown in figure 1, approximating the boundary of the eyelids from a digital photo. The eye surface is treated as flat because the radius of curvature of the eye surface is much larger than the tear film thickness (Berger & Corrsin 1974). In recent work, the flow of a thin film has been studied on a prolate spheroid—a good approximation to the shape of the human cornea (Read *et al.* 2006)—where it was found that the ellipsoidal substrate did not have a significant effect on the thinning rate near the centre of the cornea (Braun *et al.* 2010). We note that flattening the exposed surface of the eye to a plane does underestimate the area of the surface by about 30 % as discussed by Tiffany, Todd & Baker (1998).

The coordinate directions are (x', y', z'), with velocity components of the film (u', v', w'). The tear film free surface is located at $z' = h'(x', y', t')$, where t' denotes time and primed variables indicate dimensional quantities.

The aqueous tear fluid is assumed to be an incompressible Newtonian fluid governed by the Navier–Stokes equations. The density $\rho = 10^3 \text{kg m}^{-3}$ and viscosity $\mu = 10^{-3} \text{Pa s}$

Non-dimensional scalings

$L' = 5 \times 10^{-3}$ m	x' and y' length scale
$d' = 5 \times 10^{-6}$ m	z' length scale
$U' = 5 \times 10^{-4}$ m s^{-1}	velocity scale
L'/U'	time scale

TABLE 1. The scaling used to non-dimensionalize the governing equations of motion.

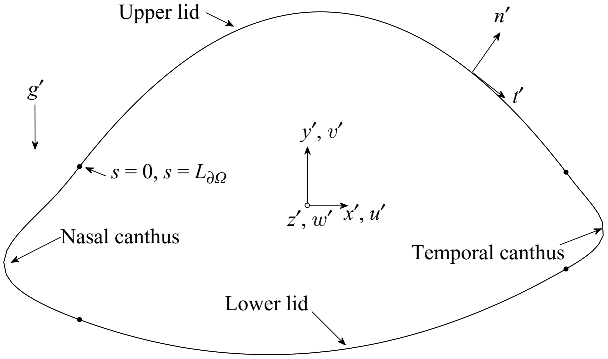

FIGURE 1. Coordinate system along with the domain for the tear film model.

are chosen to have numerical values matching pure water, because the aqueous layer is primarily composed of water (Mishima 1965; Fatt & Weissman 1992). We note that the tear fluid is shear thinning but our choice matches the high-shear rate asymptote measured in the tear fluid (Tiffany 1991). We chose appropriate boundary conditions to model the interactions of the aqueous layer with the corneal surface and the lipid layer at the free surface. The corneal/aqueous interface is simplified to be a flat, no-slip surface. At the aqueous/lipid interface, the lipid layer is assumed to render the free surface tangentially immobile as first treated by Wong *et al.* (1996). (Although we could derive this from the equations after Naire, Braun & Snow 2000 or Braun & King-Smith 2007, we simply assume it here to save space.) The surface tension at the tear/air interface is the constant value $\sigma = 45\,\mathrm{mN\,m^{-1}}$ (Miller 1969; Nagyová & Tiffany 1999).

2.1. *Thin film equation*

The full Navier–Stokes equations and boundary conditions described above are simplified via lubrication theory, which exploits the difference between the characteristic length scales in the tear film problem. In particular, the x' and y' length scale is the half-width of the palpebral fissure $L' = 5 \times 10^{-3}$ m and the z' length scale is the characteristic tear film thickness $d' = 5 \times 10^{-6}$ m. After non-dimensionalizing the governing equations with the scales shown in table 1 and expanding the dependent variables in a perturbation series in $\epsilon = d'/L'$, the leading-order approximations on $0 < z < h(x, y, t)$ and $(x, y) \in \Omega$ are

$$u_x + v_y + w_z = 0, \quad u_{zz} - p_x = 0, \quad v_{zz} - p_y - G = 0 \quad \text{and} \quad p_z = 0, \tag{2.1}$$

where p represents pressure and

$$G = \frac{\rho g d'^2}{\mu U'}, \tag{2.2}$$

with $g = 9.81\,\mathrm{m\ s^{-2}}$. As for the boundary conditions, on the surface of the eye $z = 0$ we have

$$u = v = w = 0. \tag{2.3}$$

On the free surface $z = h(x, y, t)$, we have the kinematic, normal stress and tangential immobility conditions given by, respectively,

$$w = h_t + uh_x + vh_y, \quad -p = S\nabla^2 h \quad \text{and} \quad u = v = 0, \tag{2.4}$$

where

$$S = \frac{\sigma\epsilon^3}{\mu U'}. \tag{2.5}$$

Note that $\nabla = \hat{\boldsymbol{\imath}}\partial/\partial x + \hat{\boldsymbol{\jmath}}\partial/\partial y$ and $\nabla^2 = \partial^2/\partial x^2 + \partial^2/\partial y^2$. The above equations can be combined into the single evolution equation of the form

$$h_t + \nabla\cdot\boldsymbol{Q} = 0, \tag{2.6}$$

with $\boldsymbol{Q}$ denoting the fluid flux. From lubrication theory, we find

$$\boldsymbol{Q} = -\frac{h^3}{12}\nabla\left(-S\nabla^2 h + Gy\right). \tag{2.7}$$

For the tear film, $S \approx 10^{-5}$ is the ratio of surface tension to viscous forces and $G \approx 0.05$ is the ratio of gravity to viscous forces. For computation, it will be convenient to write (2.6) as a system:

$$h_t + \nabla\cdot\left[-\frac{h^3}{12}\nabla(p + Gy)\right] = 0, \tag{2.8}$$

$$p + S\nabla^2 h = 0. \tag{2.9}$$

2.2. *Eye-shaped domain*

The boundary is divided into four parts each parametrized by the Cartesian variable for which it is single valued (the four regions are separated by dots in figure 1). The upper and lower lids are second-degree polynomials whose coefficients are found by a least squares fit to selected points along the eyelids from a digital photo of a fully open left eye taken by us. Capture of points on the lid margin may be done manually or via edge detection using, for example, the image processing toolbox in MATLAB (The MathWorks Inc.). The temporal and nasal curves are ninth-degree polynomials that smoothly patch together the upper and lower lids. The coefficients are found by matching the function value and the first four derivatives at each end point. Detailed expressions for the domain we used are given in the Appendix.

2.3. *Boundary conditions*

We specify the tear film thickness and the normal component of the flux along the boundary. The tear film thickness is assigned with the single thickness strategy on the entire boundary, $h|_{\partial\Omega} = 13$, which is in the upper end of the experimental range for the TMW (Golding, Bruce & Mainstone 1997). It is unclear if this is the correct modelling assumption for the nasal canthus because of the small, pink, globe-like nodule (*caruncula lachrymalis*) located there; however, we assume that the tear film is anchored at constant thickness all around the lid margins as a first step.

We still need another boundary condition, and we specify the flux normal to the boundary. We assume that the flux has only spatial dependence in this work; this is a drastic simplification of what occurs *in vivo* (Doane 1981), but we use this assumption

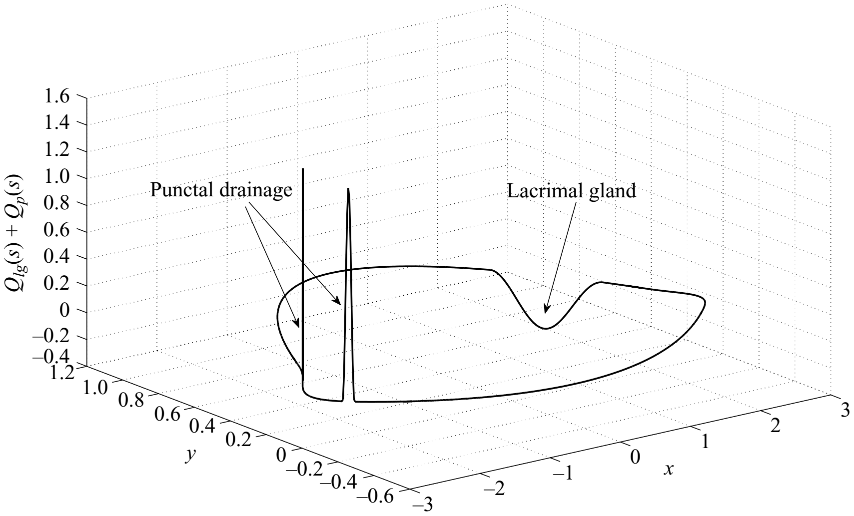

FIGURE 2. The initial flux boundary condition $Q_{lg}(s)+Q_p(s)$. The parameters are given in table 2. Outside the punctal drainage and lacrimal supply areas, the flux is specified to be zero at the boundary.

as a beginning. Let s denote the arclength of the eye-shaped boundary curve, where $s=0$ and $s=L_{\partial\Omega}$ correspond to the intersection of the top lid curve and the nasal canthus curve (see figure 1). We study both no-flux and non-zero flux boundary conditions. In the no-flux strategy, the outward normal boundary flux is simply

$$(\boldsymbol{Q}\cdot\boldsymbol{n})(s)=0. \tag{2.10}$$

In the non-zero flux case, the outward normal direction of the boundary flux is given by

$$(\boldsymbol{Q}\cdot\boldsymbol{n})(s)=Q_{lg}(s)+Q_p(s), \tag{2.11}$$

where $Q_{lg}(s)$ models the influx from the lacrimal gland and $Q_p(s)$ is associated with puncta drainage. For the lacrimal gland, we use the following continuous piecewise function

$$Q_{lg}(s)=\begin{cases}0 & \text{if } s<s_{lg,on}-\Delta s_{lg}\\ -\dfrac{1}{2}Q_{0lg}\left[\cos\left(\dfrac{\pi}{2}\dfrac{s-s_{lg,on}}{\Delta s_{lg}}-\dfrac{\pi}{2}\right)+1\right] & \text{if } |s-s_{lg,on}|\leqslant\Delta s_{lg}\\ -Q_{0lg} & \text{if } s_{lg,on}+\Delta s_{lg}\leqslant s\leqslant s_{lg,off}-\Delta s_{lg}\\ -\dfrac{1}{2}Q_{0lg}\left[\cos\left(\dfrac{\pi}{2}\dfrac{s-s_{lg,off}}{\Delta s_{lg}}-\dfrac{\pi}{2}\right)+1\right] & \text{if } |s-s_{lg,off}|\leqslant\Delta s_{lg}\\ 0 & \text{otherwise.}\end{cases} \tag{2.12}$$

Note that $Q_{lg}(s)$, shown in figure 2, is negative because $\boldsymbol{n}$ is the outward normal vector. Unless otherwise stated, the parameters are given in table 2, and the coefficient Q_{0lg} is chosen such that

$$\int_0^{L_{\partial\Omega}}|Q_{lg}(s)|\,\mathrm{d}s=Q_{mT}.$$

The parameter Q_{mT} is the non-dimensional steady supply from the lacrimal gland, which is computed from the estimate of $1.2\,\mu\mathrm{l\,min}^{-1}$ from Mishima *et al.* (1966).

Parameter	Description	Value
Q_{mT}	Estimated steady supply from lacrimal gland	0.16
Q_{0p}	Height of punctal drainage peak	$Q_{mT}/(s_{lg,off}-s_{lg,on})$
Q_{0lg}	Height of lacrimal gland peak	$Q_{mT}/\Delta s_p$
$s_{lg,on}$	On-ramp location for lacrimal gland peak	4.2
$s_{lg,off}$	Off-ramp location for lacrimal gland peak	4.6
Δs_{lg}	On-ramp and off-ramp width of lacrimal peak	0.2
p_{out}	Fraction of drainage from upper punctum	0.5
$s_{p,lo}$	Lower lid punctal drainage peak location	11.16
$s_{p,up}$	Upper lid punctal drainage peak location	11.73
Δs_p	Punctal drainage peak width	0.05

TABLE 2. Values of the non-dimensional parameters introduced in (2.12) and (2.13). Unless otherwise stated, these values were used in all simulations discussed in § 4.

On the other hand, the punctal drainage is given by

$$Q_p(s)=\begin{cases}0 & \text{if } s<s_{p,lo}-\Delta s_p\\ -\dfrac{Q_{0p}}{2}(1-p_{out})\left[\cos\left(\pi\dfrac{s-s_{p,lo}}{\Delta s_p}-\pi\right)-1\right] & \text{if } |s-s_{p,lo}|\leqslant \Delta s_p\\ 0 & \text{if } s_{p,lo}+\Delta s_p\leqslant s\leqslant s_{p,up}-\Delta s_p\\ -\dfrac{Q_{0p}}{2}(p_{out})\left[\cos\left(\pi\dfrac{s-s_{p,up}}{\Delta s_p}-\pi\right)-1\right] & \text{if } |s-s_{p,up}|\leqslant \Delta s_p\\ 0 & \text{otherwise.}\end{cases} \tag{2.13}$$

The fluxes from punctal drainage are distributed between the lower and upper lids by the parameter p_{out}. Unless otherwise stated, the parameters are given in table 2, and the coefficient Q_{0p} is such that

$$\int_0^{L_{\partial\Omega}} |Q_p(s)|\,\mathrm{d}s = Q_{mT}. \tag{2.14}$$

Here we have chosen the drainage through the puncta to match the influx from the lacrimal gland. The flux boundary condition is plotted in figure 2, where both the supply and lacrimal drainage are localized to physiologically realistic locations.

2.4. *Initial condition*

The initial condition we use is

$$h(\boldsymbol{x},0)\equiv g(x,y)=(h_0-1)\,\mathrm{e}^{-min(\mathrm{dist}(\boldsymbol{x},\partial\Omega))/x_0}+1, \tag{2.15}$$

where $x_0=0.06$ and $\mathrm{dist}(\boldsymbol{x},\partial\Omega)$ denotes the distance between $\boldsymbol{x}$ and a point on the boundary $\partial\Omega$. For this choice, the initial tear film volume is 2.45 µl. Mishima *et al.* (1966) estimated the exposed tear volume to be 4.0 µl, while Mathers & Daley (1996) experimental measurements range from 2.23 ± 2.5 µl found by measuring fluorescein concentration. We chose to make the initial condition match the estimated tear volume found by Mathers & Daley (1996) in this paper. Ideally, we are interested in simulating an initial condition constructed with $x_0=0.01$ because the initial TMH falls in the range of measured experimental values. Given the current strategy for assigning the initial condition, it does not seem possible to satisfy both an experimental TMH value and volume estimate. We note that Tiffany *et al.* (1998) computed that the exposed area of the eye surface is 30 % larger than a two-dimensional projection such as in a

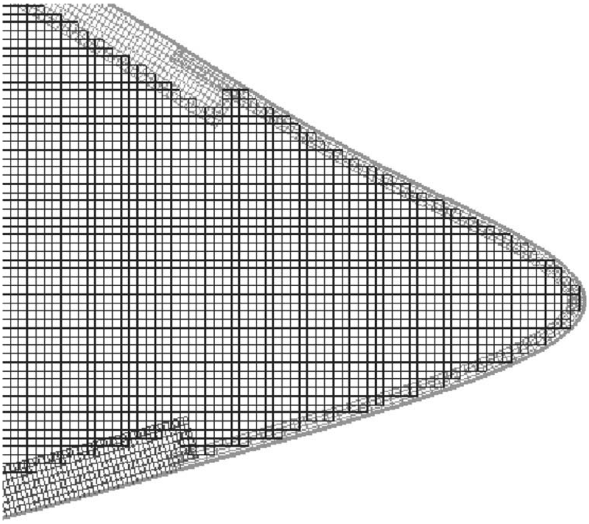

FIGURE 3. The temporal corner of the composite overlapping grid of the eye-shaped domain. The uppermost and lowermost grids follow the lower and upper lid margins, respectively, to the nasal canthus. In the nasal canthus, there is a similar curvilinear boundary-fitted grid. A uniform grid aligned with the coordinate axes is used away from the boundaries.

photograph. Using an approximately 30 % reduction in the volume from the interior region of the tear film, which mimics the reduction in area, may help the situation for computational models; since most tear volume is in the menisci, the improvement may be limited. We will investigate this possibility in future work.

3. Numerical method

The numerical method as well as the composite grid is the same as described in Maki *et al.* (2010) and the only new feature is the enforcement of the flux boundary condition. The system (2.8) is solved using an implementation of the method of lines. The spatial derivatives are approximated by curvilinear finite differences, which results in a system of differential-algebraic equations (DAE), and an adaptive second-order backward differentiation formula (BDF) time stepping method (after Brenan, Campbell & Petzold 1989) is used to advance the solutions. The flux boundary condition only specifies the flux in the normal direction and incorporating the flux boundary condition into the discretized system required some care; details and the results of numerical tests are given in the Appendix.

3.1. *Overset grid method*

The eye-shaped domain is discretized using composite overlapping grids. A composite overlapping grid is a collection of component grids, each logically rectangular curvilinear, covering a domain and overlapping where they meet. The solutions on the different component grids are coupled via interpolation conditions. For our problem, the composite overlapping grid is composed of boundary-fitting curvilinear grids at the lid margins with a background Cartesian grid for the remaining area. To construct the eye grid, we use the grid generation capabilities of the OVERTURE computational framework developed at Lawrence Livermore National Laboratory (Chesshire & Henshaw 1990; Henshaw 2002). Figure 3 displays the grid in the temporal canthus. Each boundary curve is defined by non-uniform rational B-spline

t	h_{min} $G=0$	h_{min} $G=0.05$
0	1	1
1	0.7242	0.7696
2	0.5203	0.5997
5	0.3220	0.4434
15	0.1783	0.0639

TABLE 3. Minimum film thickness for no-flux boundary conditions at various times with and without gravity active.

(NURBS; Piegl & Tiller 1997), and a boundary-fitting grid is produced by extending the normals. Second-order accurate finite difference approximations to derivatives, constructed in the mapped domain for each composite grid, are used to approximate spatial derivatives at grid points. Additional detail is given in the Appendix.

4. Tear film dynamics

We give results for the no-flux condition, followed by results for the non-zero flux condition. The former gives us a test case for conserving mass during the computation, and a good contrast for understanding the supply and removal of tear fluid that occurs in the second case.

4.1. *No-flux boundary condition*

The dynamics are first considered with $G=0$, and subsequently $G=0.05$. By comparing the two different cases, we can better understand the influence of gravity in the model. The absence of gravity could be interpreted as a subject being supine or as gravity being negligible in the dynamics of the tear film (e.g. Wong *et al.* 1996; Creech *et al.* 1998). However, we shall see that gravity influences the flow around the lid margins in our model.

4.1.1. *Capillarity only*

Figure 4(a) shows the dynamics of the tear film contours. The dominant feature is the capillarity-driven thinning of the film that creates the so-called black line adjacent to the menisci. The black line is a thin region of tear fluid that fluoresces much less than the rest of the tear film when fluorescein dye is added to the tear film in the presence of a blue light source. In the computation, the black line forms rapidly and emerges as a dark blue band in figure 4. The feature driving the thinning is the highly curved menisci. The tear fluid near the menisci is sucked into the menisci, because the large thickness at the boundary creates a positive curvature in the film surface and hence a low pressure. The low-pressure regions near the boundary are shown at two different times in figure 5. The global minimum develops at the intersection of the black lines in the nasal canthus. In general, the thinning dynamics slow down as time increases as shown in the minimum tear film thickness values. The global minimum for the thickness occurs near the nasal canthus and those values for several times are given in table 3.

The black line separates the tear fluid in the menisci and the interior. A ridge forms in the interior (the light turquoise band in figure 4), which is not as pronounced as in the pressure boundary cases (Maki *et al.* 2010). At the intersection of the ridges in the canthi regions are the local maxima. As time evolves, the inward movement of

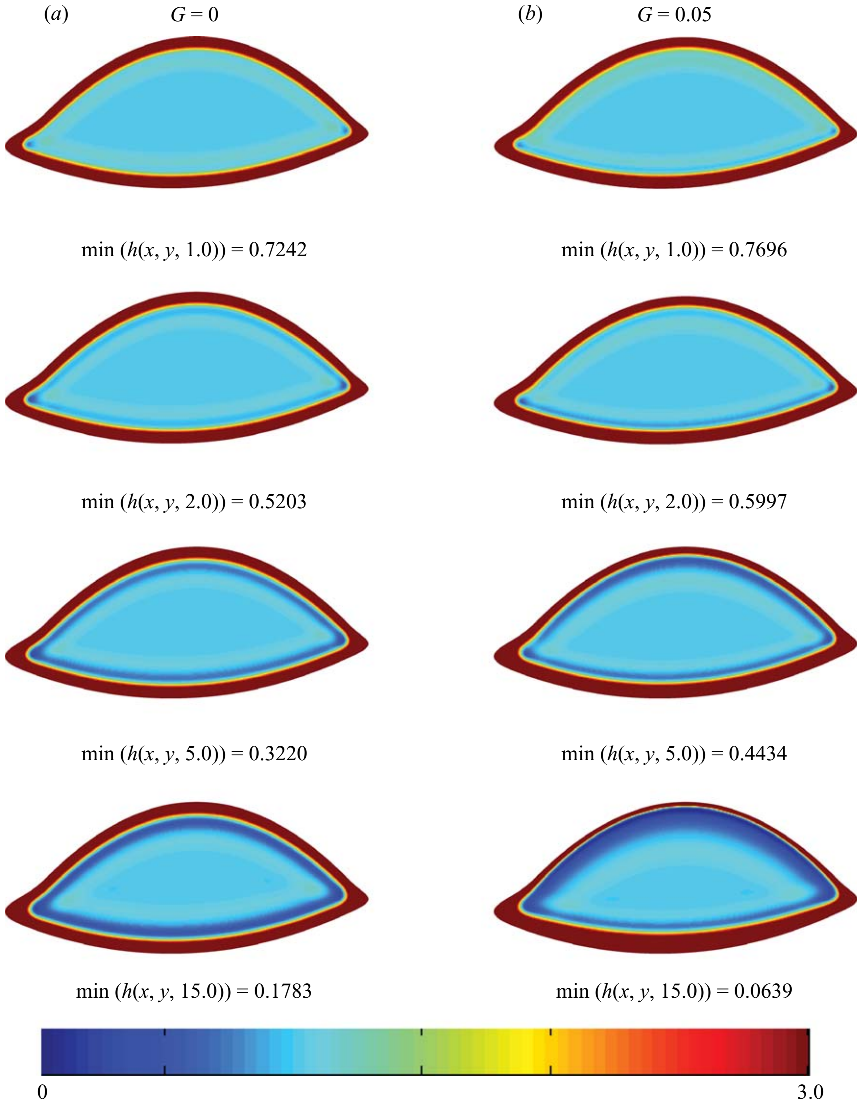

FIGURE 4. A time sequence of the contour plots of the tear film thickness, with the no-flux boundary condition. Note that the maroon regions indicate tear film thickness greater than or equal to 3.

the light turquoise region illustrates the slow spreading of the ridge away from the black line.

Figure 5 shows the behaviour of the pressure. The lower pressure in the menisci remains throughout the simulation. The low-pressure menisci themselves evolve towards a constant-valued pressure configuration. With only the normal pressure gradient being constrained by the flux boundary condition, the value and shape of the pressure in the menisci changes with time. The pressure is elevated in the interior and separated from the low-pressure menisci. These rapid pressure changes follow the boundary and intersect near the canthi. But, the severity of the rapid change lessens with increasing time and becomes smoother. In the interior, the elevated

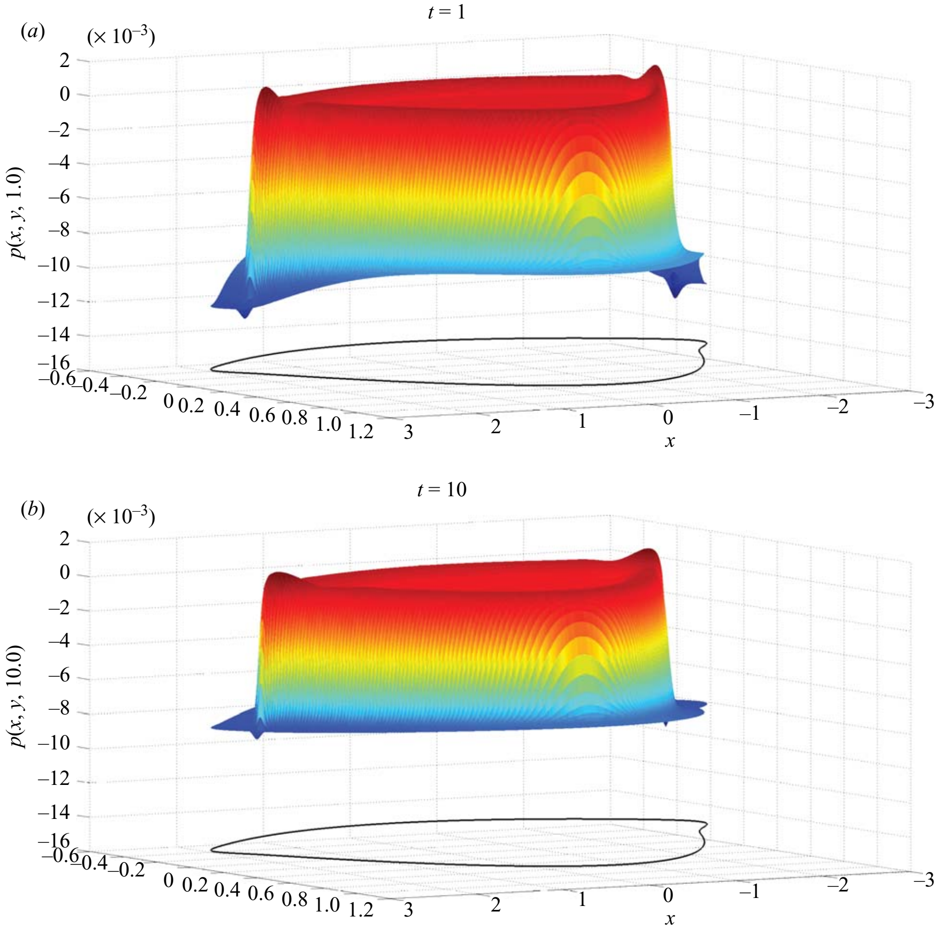

FIGURE 5. A time sequence of the pressure with $G = 0$ and the no-flux boundary condition. The coloured surface is the pressure and the curve beneath the pressure surface is the edge of the domain shown for reference. Note that the direction of view is from the location of the lacrimal gland so that the temporal canthus is on the left and the nasal canthus is on the right.

pressure distribution in the canthi regions, if viewed normal to the surface of the eye, resembles a wedge with smoothed corners.

We use the error in volume conservation as an indicator of the numerical accuracy of the computed solution (though it is not a bound; see Maki *et al.* 2008). The volume at time t is given by

$$V(t) = \int_{\Omega} h(x, y, t)\,\mathrm{d}A, \tag{4.1}$$

and the error in volume conservation is $E_V(t) = |V(t) - V(0)|$, where $V(0)$ is the initial volume with non-dimensional value of 14.44. The error is at most $E_V(10) = 0.05$, corresponding to 0.35 % of the initial non-dimensional tear volume.

To examine the hydraulic connectivity in our model, we display the flux of the tear fluid during the interblink period in figures 6 and 7. The flux direction field is plotted over the contours of the norm of flux, where the grey scale is such that dark regions indicate a small flux and white corresponds to $\|\boldsymbol{Q}\| \geqslant 10^{-2}$. We note that in all flux

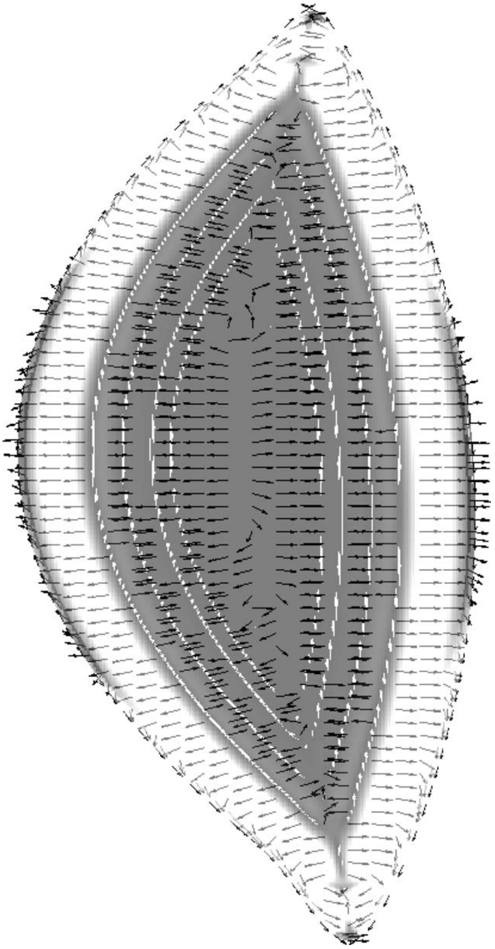

FIGURE 6. The flux direction field plotted over the contours of the norm of the flux at $t = 1$. The boundary condition is no-flux and $G = 0$. In the upper and lower menisci, the location of the switch in the direction of flow is in the dark region.

figures, the amount and distribution of the arrows does not reflect properties of the computational grid (there are far fewer arrows than grid points for clarity). The flux magnitude in the menisci and canthi regions is greater than or equal to the interior flux. In general, the menisci and canthi regions contain more tear fluid allowing for more mobility. As time increases, the tear fluid collects in the canthi regions, thus causing the maroon band in the nasal canthus in figure 4 to widen.

The tear fluid flows along the boundary towards the lower-pressure canthi regions and nowhere through it because of the no-flux condition. Note that the interior flux vectors near the upper lid in figure 6 that point outward are not boundary vectors. In the interior, the top of the ridge separates the fluid flow into and out of the interior. Although the tear fluid does collect in the canthi regions, the tear fluid does not travel from the upper meniscus into the lower meniscus as in the experiments of Harrison *et al.* (2008), and therefore, we conclude that this simulation does not capture hydraulic connectivity.

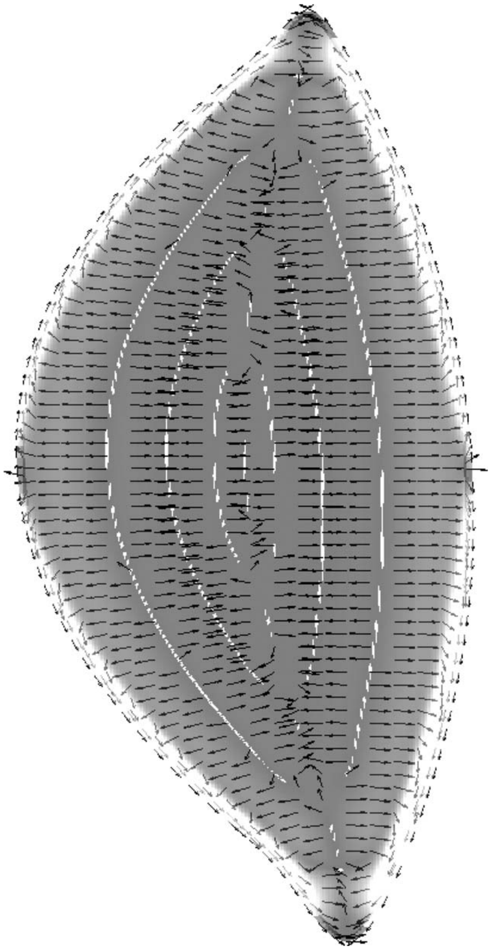

FIGURE 7. The flux direction field plotted over the contours of the norm of the flux at $t = 10$. The boundary condition is no-flux and $G = 0$. The flux stagnates in regions where the boundary has local maxima in its curvature.

To better understand how tear fluid is redistributed from the menisci to the canthi, we first note that in an equilibrium meniscus shape the pressure (or curvature in our thin film approximation) is constant. In general, the tear film in the menisci evolves towards such an equilibrium shape. Therefore, consider the tear film thickness at the fixed grid point $x_{i,j}$ where $\mathrm{dist}(\boldsymbol{x}, \partial\Omega) = \epsilon$ and $\epsilon > 0$. Suppose that the equilibrium shape of the meniscus is such that $\nabla^2 h = C$, where C is a constant, and consider the dependence of $h_{i,j}$ on the curvature of $\partial\Omega$. Recall that we can interpret $\nabla^2 h$ as

$$\begin{aligned}\nabla^2 h(x_0, y_0, t_0) \approx{} & \text{average value of } h \text{ in the neighbourhood of } (x_0, y_0) \\ & - h(x_0, y_0, t_0).\end{aligned} \tag{4.2}$$

If the nasal canthus boundary curve is $\partial\Omega_2$ as in figure 8, then we have $h_{i,j+1} = h_{i,j-1} = h_{i-1,j} = h_0$ because of the thickness boundary condition. Moreover, if we let $(h_{i,j-1} + h_{i,j+1} + h_{i-1,j})/3$ approximate the average value of h in the neighbourhood, then by (4.2),

$$C \approx h_0 - h_{i,j}. \tag{4.3}$$

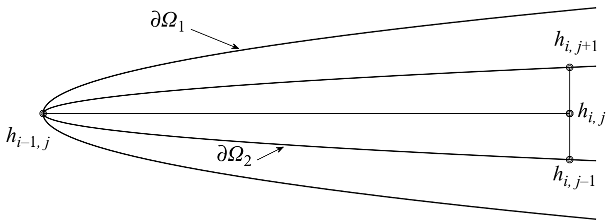

FIGURE 8. An example of the nasal canthus boundary curve with different curvatures.

On the other hand, if the nasal boundary curve is $\partial\Omega_1$, then $h_{i-1,j} = h_0$, $h_{i,j-1} = h_0 - \epsilon_1$ and $h_{i,j+1} = h_0 - \epsilon_2$, where $\epsilon_1 > 0$ and $\epsilon_2 > 0$, then

$$C \approx h_0 - \epsilon_1/3 - \epsilon_2/3 - h_{i,j}. \tag{4.4}$$

Therefore, to achieve an equilibrium shape with curvature C, the thickness a fixed distance ϵ away from a higher-curvature boundary must be larger (via (4.3)) than the thickness a fixed distance ϵ away from a smaller-curvature boundary (via (4.4)).

4.1.2. *Capillarity and gravity*

The presence of gravity redistributes the tear film from the top (near the upper lid) to the bottom. The global behaviour of the redistribution is clearly shown in figure 4, where a time sequence of the tear film thickness contours are plotted for $G = 0$ (figure 4*a*) and $G = 0.05$ (figure 4*b*). The black line is still created at early times, but now the black lines near the upper and lower menisci have different minimum thicknesses. Near the upper meniscus, there is a competition between capillarity, which draws fluid into the meniscus, and gravity, which pulls fluid down the surface of the eye. However, near the lower meniscus, gravity accelerates the formation of the black line because it cooperates with capillarity there. At $t = 1$ (figure 4*b*) near the upper meniscus, the absence of the blue band illustrates the competition, whereas the presence of the dark blue band near the lower meniscus illustrates the acceleration when compared to figure 4(*a*).

Because no tear fluid can exit the domain, the tear fluid flows from the upper meniscus into the lower meniscus and accumulates in the centre of the lower meniscus. As a result, the upper TMH decreases and the lower TMH increases. The opposite occurred in the pressure boundary condition case (Maki *et al.* 2010). The inward spreading of the interior ridge near the upper lid is accelerated by gravity and hindered near the lower lid.

The dynamics of the pressure distribution are shown in figure 9. The distributions include the elevated pressure region remaining separated from the low-pressure menisci and the pressure distributions in the menisci changing with time. The pressure distribution in the meniscus appears to be linear in y which indicates a hydrostatic component of the pressure.

Including the effect of gravity promotes hydraulic connectivity in the no-flux model (see figure 10). In particular, gravity accelerates the tear flow in the upper meniscus towards the canthi regions and removes the previous dark or slower region at the tear flow split (in the middle of the upper and lower lids). Gravitational acceleration causes the upper TMH to decrease with time (see figure 4). When gravity is active, the tear fluid no longer collects in the canthi regions, but rather flows into the lower meniscus where the direction of the tear flow is such that the tear fluid collects in the centre of the lower meniscus. In the interior, the flux always points downward.

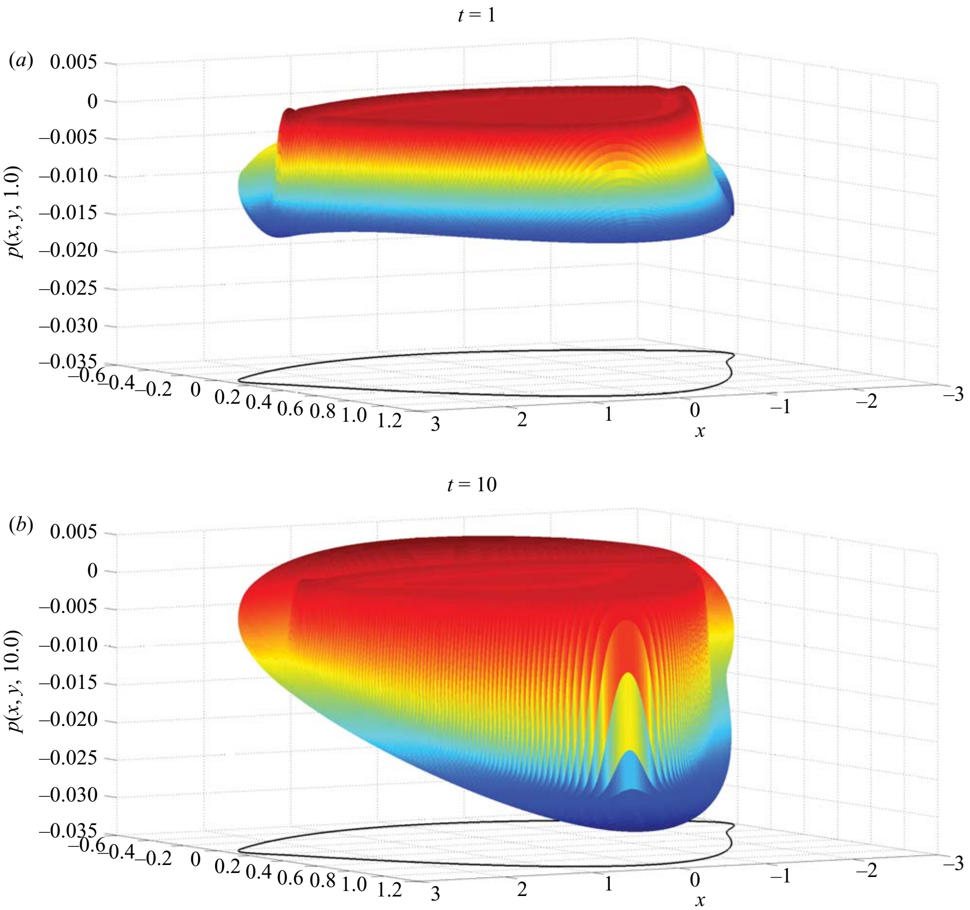

FIGURE 9. A time sequence of the tear film pressure with $G = 0.05$ and the no-flux case. Note the sharpening separation between the high-pressure centre and low-pressure meniscus with increasing time. The viewpoint is from the direction of the lacrimal gland (from the superior and temporal direction).

4.2. *Non-zero flux boundary condition*

4.2.1. *Capillarity only*

In this section, we explore the effects of the non-zero flux boundary condition plotted in figure 2 with $G = 0$. Consider the dynamics of the tear film thickness contours plotted in figure 11(*a*). At $t = 1$, the contour plots of the thickness with non-zero flux (see figure 11) and no-flux (see figure 4) look nearly identical. Because of the presence of the menisci, the meniscus-driven thinning creates the black line with the minimum again occurring in the nasal canthus region. In the non-zero flux case, the minimum is smaller than that in the no-flux case.

As time increases, the influence of the flux boundary condition becomes increasingly apparent in the menisci and canthi regions. The upper TMH (e.g. the width of the maroon band) around the influx slowly lengthens and begins to bulge through the black line. In contrast, in the nasal canthus around the punctal drainage, the TMH steadily decreases. The black line is persistent throughout the calculation, but its minimum thickness is smaller in the nasal canthus (see the dark blue region), and its

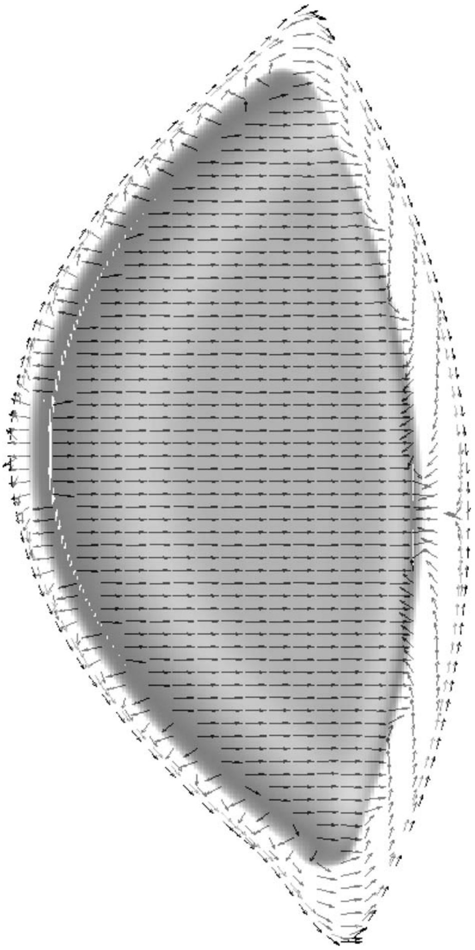

FIGURE 10. The flux direction field plotted over the contours of the norm of the flux at $t = 10$. The boundary condition is no-flux and $G = 0.05$. The flow separates at the top, flows around the canthi and collects at the centre of the bottom lid.

minimum thickness is larger in the upper meniscus near the lacrimal influx (e.g. the lighter blue region). It is difficult for the lacrimal gland influx to break through the black line region in this relatively short simulation.

In the interior, the overall dynamics are similar to the no-flux case. An interior ridge forms and at the intersection relative maxima form in the canthi regions. Again, as time increases, the inward growth of the light turquoise band illustrates the slow spreading of the ridge away from the black line. We note that the volume is conserved because the lacrimal gland influxes match the punctal drainage. The error in volume conservation for the non-zero flux case is at most 0.69 % of the initial non-dimensional tear volume during the simulation.

Figure 12 shows the dynamics of the pressure distribution. As before, the lower pressure in the menisci remains throughout the simulation. Now, however, the difference between the elevated-pressure interior and low-pressure meniscus drastically changes with increasing time. In particular, near the lacrimal gland influx, the separation decreases as the meniscus bulges with excess tear fluid and the curvature decreases. On the other hand, near the puncta, the separation increases severely as

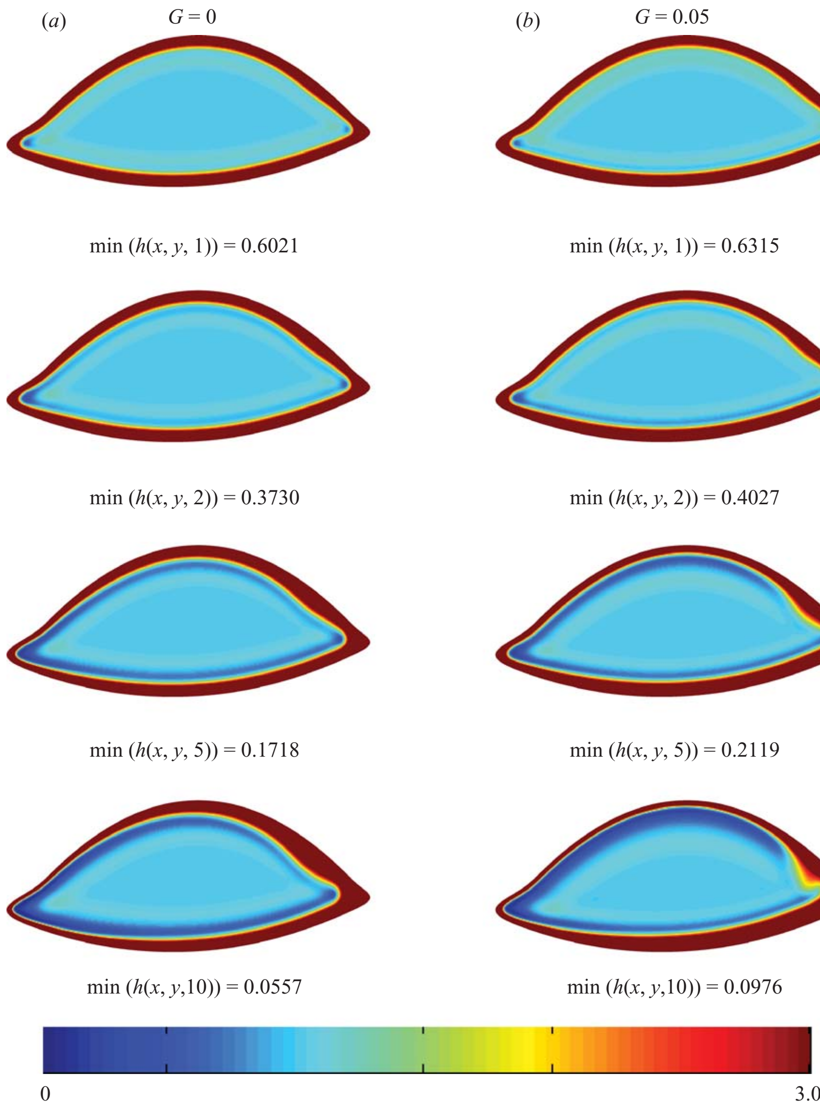

FIGURE 11. A time sequence of the contour plots of the tear film thickness, with the non-zero flux boundary condition and $G = 0$ (*a*) or $G = 0.05$ (*b*), illustrating the global behaviour. Note that the maroon regions indicate tear film thickness greater than or equal to 3.

the meniscus loses tear fluid and the curvature increases. The development of the sharp separation in the nasal canthus limits the time for which we can compute solutions. Similar to the pressure boundary condition cases in Maki *et al.* (2010), the intersection of the rapid pressure changes near the nasal canthus, and if viewed from above resembles a wedge.

The dynamics of the tear film thickness and pressure along $x = 0$ are plotted in figure 13. The pressure distribution changes rapidly from $p \approx 0$ in the interior to a negative value near the boundary. In the non-zero flux case, the negative boundary pressure now increases with increasing time at this position. This allows for the slope of the rapid change in pressure distribution near the boundary to decrease in magnitude with increased time. In contrast, for the pressure boundary condition case,

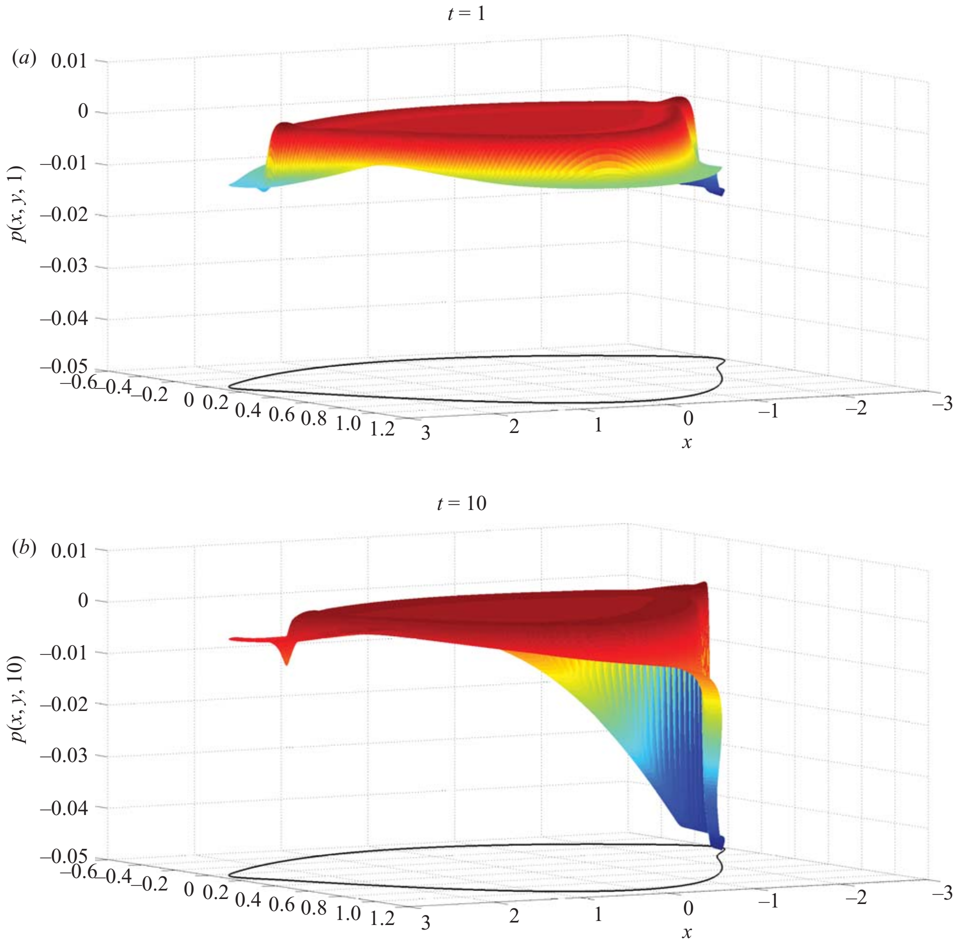

FIGURE 12. A time sequence of the pressure with $G = 0$ and the non-zero flux boundary condition. Note the development of the wedge in the nasal canthus region and the sharper separation between the elevated and low-pressure meniscus.

the pressure near the boundary evolved to a nearly vertical slope at this location (Maki *et al.* 2010); in the non-zero flux case in this section, such steepening occurs near the nasal canthus.

Figures 14 and 15 display the direction of the flux over the contour plot of the norm of the flux at $t = 1$ and $t = 10$. The first observation is that the overall interior flux dynamics, away from the menisci and canthi regions, are the same for the no-flux and non-zero flux cases. However, the tear flow in the menisci and canthi regions changes dramatically from the no-flux to the non-zero flux case. The effects of lacrimal gland influx and the punctal drainage are now clearly visible as there is flow through the boundary.

The lacrimal gland influx splits with some tear fluid travelling through the upper meniscus and some travelling around the temporal canthus and into the lower meniscus. At $t = 1$, the effects of the boundary fluxes are not felt everywhere. The tear flow in the upper and lower menisci away from the fluxes behaves like the no-flux case. That is, the direction of the tear flow in the dark region at the top of the upper meniscus splits so that some tear fluid travels towards the nasal canthus and

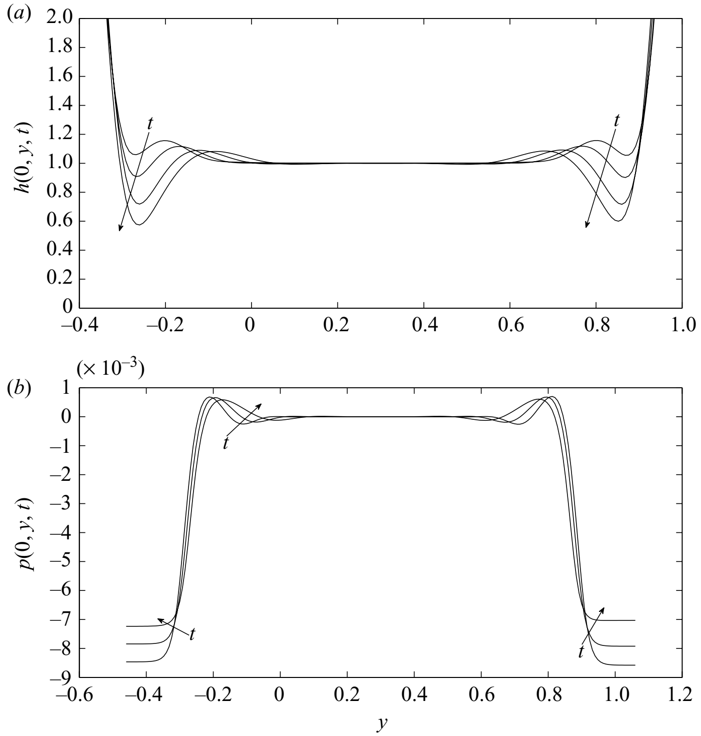

FIGURE 13. A time sequence of the tear film thickness (*a*) and pressure (*b*) along $x = 0$ with $G = 0$ and the non-zero flux boundary condition.

some travels towards the temporal canthus. By $t = 10$, the tear flow everywhere in the lower meniscus points towards the lower punctum, and in the upper meniscus, the tear fluid to the nasal side of the split flows towards the upper punctum. Thus, it takes around 10 s for the lacrimal gland influx to change the tear flow pattern in both menisci favouring travel through the menisci toward the puncta. This time scale appears to be slower than the description of Maurice (1973), but it is not at odds with the observations of Harrison *et al.* (2008). We conclude that the non-zero flux case captures some of the aspects of hydraulic connectivity.

4.2.2. *Capillarity and gravity*

In the non-zero flux case, gravity again redistributes the tear fluid from top to bottom (see figure 11). We observe similar dynamics as for the no-flux case in the interior; gravity pulls the ridge across the eye. For the previous case with $G = 0$ and non-zero flux, recall that away from the lacrimal gland influx in the upper meniscus, the tear flow behaved like the no-flux case (see figure 14). That is, the direction of the tear flow in the dark regions at the top and bottom split so that some tear fluid travelled towards the nasal canthus and some travelled towards the temporal canthus. Here gravity accelerates the no-flux behaviour. In particular, the change of direction located in the dark region at the top (the upper meniscus shown in figure 14) is now coloured white (large flux magnitude) with the tear flow still splitting and travelling towards both canthi (see figure 16). The acceleration of the no-flux boundary effects causes the upper TMH to decrease away from the lacrimal gland influx.

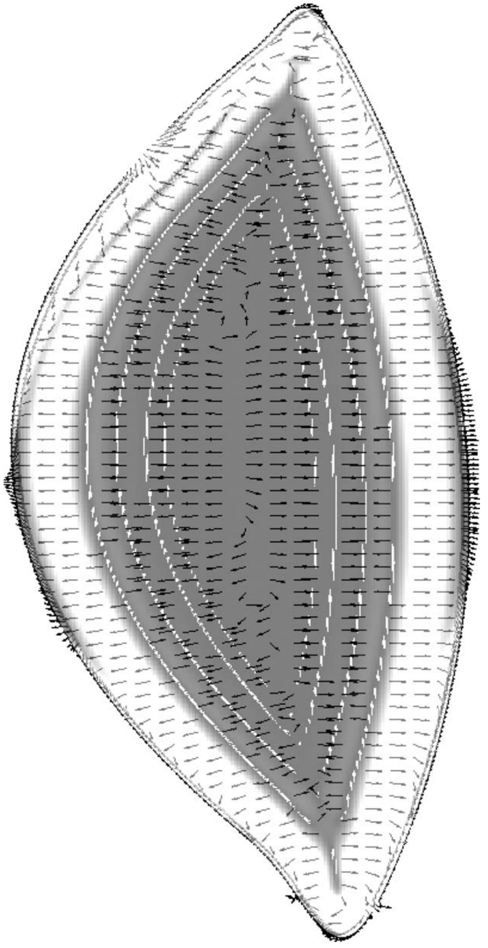

FIGURE 14. The flux direction field, with the non-zero flux boundary condition and $G = 0$, plotted over the contours of the norm of the flux at $t = 1$. Note that the direction of tear flow in the lower meniscus is not always towards the lower punctum.

Near the lacrimal gland influx, gravity pulls the bulge in the upper meniscus down the surface of the eye. As time increases, the bulge of the tear film begins to penetrate the black line region as in the one-dimensional reflex tearing study of Maki *et al.* (2008). Because of gravitational effects, the lacrimal gland influx no longer splits and travels through both menisci. As shown in figures 16 and 17, the lacrimal gland influx travels only through the temporal canthus and into the lower meniscus with gravity accelerating the flow of the lacrimal gland influx into the lower meniscus. The excess tear fluid accumulates and increases the lower TMH. A comparison of the lower meniscus in figures 14 and 16 reveals that gravity speeds up the transition of the tear flow pattern into one that favours travel through the meniscus and out the lower punctum.

This simplified model with the non-zero flux boundary case condition and gravity captures some aspects of hydraulic connectivity. What is missing is the flow towards the upper punctum in the upper meniscus. If we attempt to reproduce the experiment of Harrison *et al.* (2008) and trace the tear flow based on the flux plots, then all the

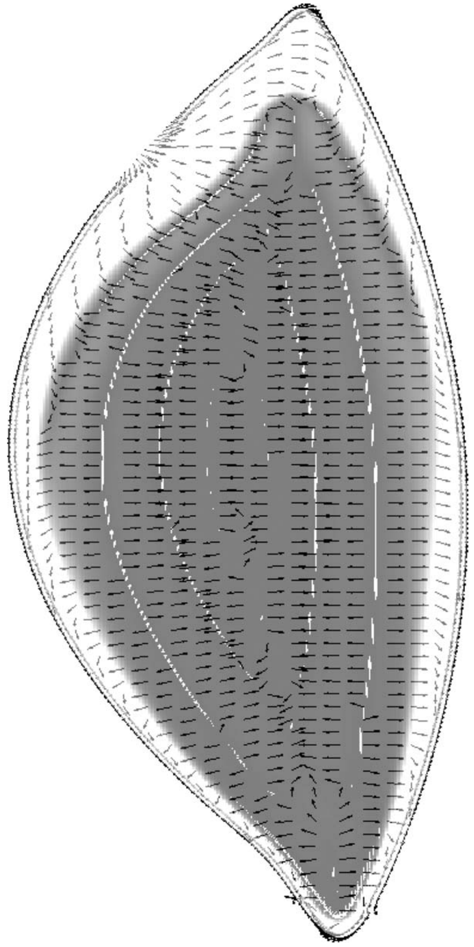

FIGURE 15. The flux direction field, with the non-zero flux boundary condition and $G=0$, plotted over the contours of the norm of the flux at $t=10$.

tear film would be channelled into the lower meniscus through the temporal canthus and none would travel around the upper meniscus in this case.

In an attempt to recover the splitting of lacrimal gland influx, we shifted the lacrimal gland inlet towards the nasal canthus (Maki 2009, results not shown). The parameters in $Q_{lg}(s)$ associated with the location of the on-ramp change to $s_{lg,on}=3.8$, and the location of the off-ramp is $s_{lg,off}=4.2$. In the upper meniscus, gravity's pull continued to overcome the lacrimal gland influx and erase the splitting effect there. The change in the lacrimal gland inlet did shift the upper meniscus split towards the temporal canthus, and therefore, closer to the lacrimal gland influx. In the unshifted flux case, the split in the upper meniscus tear flow occurred at $x=0.7062$ (figure 17), whereas now the split occurs at $x=1.0397$. The latter split is still away from the lacrimal gland inlet which lies in the interval $1.26 \leqslant x \leqslant 1.99$.

5. Discussion

The relaxation model of the tear film on an eye-shaped domain was numerically simulated with tear film thickness and flux boundary conditions. In the OVERTURE

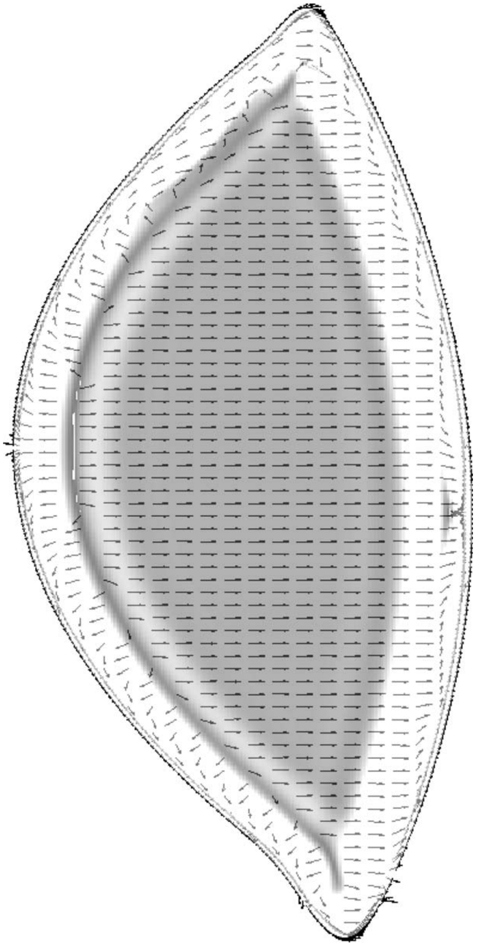

FIGURE 16. The flux direction field plotted over the contours of the norm of the flux at $t = 1$. The boundary condition is non-zero flux and $G = 0.05$.

computational framework, we implemented the overset grid method detailed by Maki *et al.* (2010) with modification to enforce the flux boundary condition as detailed in the Appendix (see also Maki 2009). We explored the effects of the geometry of the eye-shaped domain, gravity and boundary fluxes on the dynamics of the tear film thickness and the tear fluid flow.

In all of the computations reported here, we found recurring dynamics due to the consistent presence of the menisci coupled to the same thickness boundary condition. In particular, the formulation of the black line is persistent. Stronger capillary action in the vicinities of the nasal and temporal canthi regions produced local minima at the intersection of the black lines. In the dynamics of the pressure, the low-pressure menisci remained throughout each simulation.

We found that the different flux boundary conditions significantly influence the behaviour in the menisci and canthi regions. In general, the upper meniscus around the lacrimal gland influx contained more tear fluid, whereas in the nasal canthus near the punctal drainage, the meniscus contained less fluid. The excess tear fluid found near the lacrimal gland influx decreases the curvature, and therefore, increases the pressure. In a similar manner, the lack of tear fluid near the puncta increases

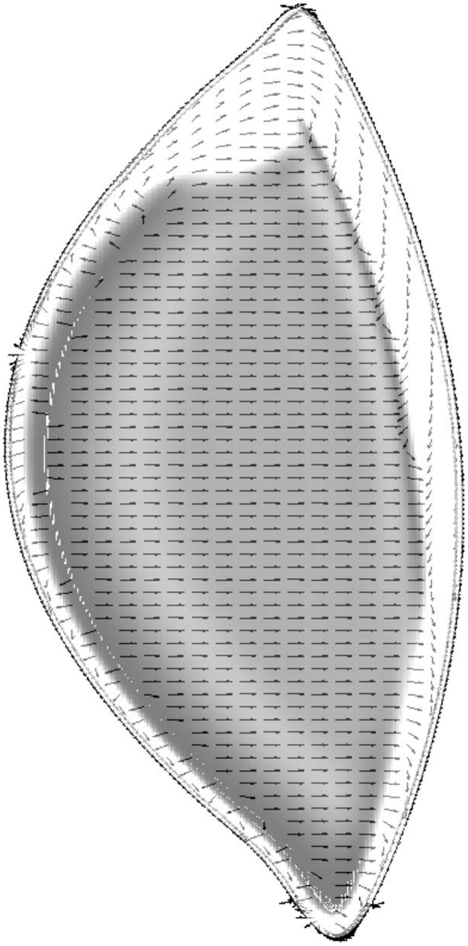

FIGURE 17. The flux direction field plotted over the contours of the norm of the flux at $t = 10$. The boundary condition is non-zero flux and $G = 0.05$.

the curvature causing the pressure to decrease. Near the puncta, the decrease in pressure continues with increasing time, eventually producing a sharp separation in the pressure that can no longer be accurately approximated by our approach (see figure 12). The sharp separation in the pressure develops faster in the non-zero flux boundary condition case stopping the calculation earlier than in previously computed pressure boundary condition cases (Maki *et al.* 2010). This behaviour agrees with some expected behaviour of pressure versus flux boundary conditions as discussed by Bertozzi *et al.* (1994). In particular, they found that for a specific flux boundary condition, referred to as the current boundary condition, a finite time singularity always occurs; on the other hand, for a specific pressure boundary condition, a singularity always forms either in finite or infinite time. An improved boundary condition, which would be closer to *in vivo* behaviour, would only have punctal drainage for a short time and thus avoid the singular pressure behaviour.

In all cases, gravity was found to redistribute the tear film from top to bottom. In particular, gravity accelerated the tear fluid flow in the upper meniscus through the canthi regions and into the lower meniscus resulting in thinner upper TMHs and thicker lower TMHs. In the interior, the spreading of the upper ridge is accelerated, while the spreading of the lower ridge is hindered. With the non-zero flux boundary case, the upper meniscus bulge is drained down the surface of the eye and begins to penetrate the black line region.

The direction of the tear flow was found to be affected by both the flux boundary condition and gravity. With capillarity only, the tear fluid in no-flux boundary case flowed into the canthi regions and collected there. On the other hand, the non-zero flux case at later time exhibited hydraulic connectivity, with the lacrimal gland influx splitting and then travelling both through the upper meniscus into the upper punctum and through the lower meniscus into the lower punctum. With gravity active, hydraulic connectivity was promoted in the no-flux boundary case, with the tear fluid in the upper meniscus travelling through the canthi regions and collected in the lower meniscus. In the non-zero flux case, gravity erases the splitting of the lacrimal gland influx.

In conclusion, we found the overall tear flow to be controlled by the menisci on the eye-shaped geometry and the flux boundary condition. The different flux boundary conditions affected only the tear film dynamics in the menisci and canthi regions, which are regions where tear film thickness and velocity are typically not measured in experiments. As may be expected, gravity was found to promote flow from the upper meniscus through the canthus and into the lower meniscus.

We have only begun to study all the possible flux boundary configurations modelling the complicated tear film drainage and supply. A natural step forward is to include time-dependent flux boundary conditions and to study the effect of moving boundaries during a blink.

This material is based upon work supported by the National Science Foundation under grant 0616483. R. J. B. thanks M. Doane for helpful conversations.

Appendix

A.1. *Boundary curves*

Each of the four boundary curves, separated by dots in figure 1, are parameterized by the Cartesian variable for which they are single valued. In particular, the upper lid is described by $y = b_U(x)$ for $-2.2 \leqslant x \leqslant 2.5$, where

$$b_U(x) = -0.13x^2 + 0.03x + 1.06. \tag{A 1}$$

The lower lid is described by $y = b_L(x)$ for $-2.2 \leqslant x \leqslant 2.5$, where

$$b_L(x) = 0.05x^2 + 0.03x - 0.45. \tag{A 2}$$

On the other hand, the temporal canthus is given by $x = b_T(y)$ for $-0.0725 \leqslant y \leqslant 0.3225$, with

$$\begin{aligned} b_T(y) = {} & -101240.64y^9 + 121085.52y^8 - 43801.57y^7 + 389.73y^6 \\ & + 2281.97y^5 - 52.09y^4 - 72.00y^3 - 10.13y^2 + 2.90y + 2.74. \end{aligned} \tag{A 3}$$

The nasal canthus is described by $x = b_N(y)$ for $-0.2840 \leqslant y \leqslant 0.3648$, where

$$\begin{aligned} b_N(y) = {} & 2660.66y^9 - 1131.49y^8 - 1272.19y^7 + 519.29y^6 \\ & + 248.43y^5 - 90.88y^4 - 30.58y^3 + 12.99y^2 + 1.17y - 2.94. \end{aligned} \tag{A 4}$$

A.2. *Overset grid method*

The evolution equation is solved using a curvilinear finite-difference-based method of lines on the composite overlapping grid described above. We use the OVERTURE computational framework to generate the curvilinear finite difference approximations. In particular, each component grid is defined by a mapping $(x(r,s), y(r,s)) = \boldsymbol{G}(r,s)$ from the unit square $(r,s) \in [0,1]^2$. Approximations to the derivatives of $h(x,y,t)$ with respect to the (x,y) are formed on the unit square (r,s) by application of the chain rule

$$h_x = r_x\tilde{h}_r + s_x\tilde{h}_s, \tag{A 5}$$

$$h_y = r_y\tilde{h}_r + s_y\tilde{h}_s, \tag{A 6}$$

$$\nabla^2 h = \left(r_x^2 + r_y^2\right)\tilde{h}_{rr} + 2(r_x s_x + r_y s_y)\tilde{h}_{rs} + \left(s_x^2 + s_y^2\right)\tilde{h}_{ss} + \nabla^2 r\tilde{h}_r + \nabla^2 s\tilde{h}_s, \tag{A 7}$$

where $\tilde{h}(r,s,t) = h(x(r,s), y(r,s), t)$ and r_x, r_y, r_{xx}, r_{yy}, s_x, s_y, s_{xx} and s_{yy} are inverse vertex derivatives computed from the mapping $\boldsymbol{G}$. The curvilinear grid finite differences are obtained by discretizing the (r,s) derivatives in (A 5)–(A 7) by centred second-order finite differences.

The time-stepping algorithm we used is a variable stepsize fixed leading coefficient implementation of the second-order backward differentiation formula. In a variable stepsize method, the general idea is to take the largest time step possible while still keeping local control over the estimated error. This fixed leading coefficient implementation was used in DASSL as described by Brenan *et al.* (1989).

A.3. *Enforcing the flux boundary condition*

In the current formulation (2.8), to enforce the normal component of the flux along the boundary we must enforce a Neumann boundary condition on the pressure. We developed new boundary condition operators in the OVERTURE computational framework for use with our model, a system that is fourth order in space. To understand the method, we consider the simplified one-dimensional model problem with exact solution $h_E(x,t)$ and $p_E(x,t)$, which generate forcing function g_E such that

$$h_t - p_{xx} = g_E(h_E(x,t), p_E(x,t)), \tag{A 8}$$

$$p + Sh_{xx} = 0, \tag{A 9}$$

on $-1 < x < 1$, with Dirichlet boundary conditions for h and Neumann for p. We consider the single uniform computational grid with spacing $\Delta x = 1/N$ and two ghost points. Let $x_j = -1 + j\Delta x$, for $j = -1, \ldots, N+1$, denote the grid points, where $h_j(t) = h(x_j, t)$, $p_j(t) = p(x_j, t)$ and $g_{E,j}(t) = g(x_j, t)$.

We need an extra equation at each boundary, depending on the pressure evaluated at the ghost point to properly approximate the problem. From (A 8) and the Dirichlet boundary condition, we obtain

$$-p_{xx} = g_E(h_E(-1,t), p_E(-1,t)) - \frac{\partial h_0}{\partial t}(t) \text{ at } x = -1. \tag{A 10}$$

	e_1^l	e_2^l	e_3^l	e_1^l/e_2^l	e_2^l/e_3^l
$l=h$	0.134	0.063	0.031	2.127	2.429
$l=p$	0.051	0.021	0.008	2.032	2.625

TABLE 4. When solving the linear model problem coupled with thickness and flux boundary conditions, the maximum absolute error of h and p at $t=1$ with $S=10^{-2}$.

When discretized, we obtain the first equation below, and the second is the discrete form of the Neumann boundary condition, viz.

$$-\frac{p_{-1}-2p_0+p_1}{(\Delta x)^2}=g_{E,0}-\frac{\partial h_0}{\partial t}(t), \tag{A 11}$$

$$\frac{p_1(t)-p_{-1}(t)}{2\Delta x}=-S\frac{\partial^3 h_E}{\partial x^3}(-1,t). \tag{A 12}$$

If we do the same at the other boundary and run a numerical experiment, then the maximum of the absolute error at $t=0.1$ is 1.8×10^{-12}. In all the computations in this paper, we enforce the normal flux boundary condition using this approach.

A.4. *Numerical grid study*

The numerical scheme described above is verified on the tear film relaxation model by a method of analytical functions. The true solution is chosen to be

$$h_E(x,y,t)=\cos(2\pi x)\cos(2\pi y)\cos(2\pi t)+2, \tag{A 13}$$

$$p_E(x,y,t)=8\pi^2 S\cos(2\pi x)\cos(2\pi y)\cos(2\pi t), \tag{A 14}$$

where S is a non-dimensional parameter. Three composite grids, G_m with $m=1,2,3$, are used to discretize the domain comprising a rectangle with a circular hole cut out, and the grid spacing is such that $(\Delta x_1 : \Delta x_2 : \Delta x_3)=(2:\sqrt{2}:1)$, approximately.

First, we consider the corresponding linear model system

$$h_t-\nabla\cdot(\nabla p)=f_E\left(h_E(x,y,t),p_E(x,y,t)\right), \tag{A 15}$$

$$p+S\nabla^2 h=0, \tag{A 16}$$

where $S=10^{-2}$, coupled with thickness and flux boundary conditions. If h_m and p_m represent the discrete solution to (A 15) on composite grid G_m at $t=1$, then the maximum absolute error is defined to be

$$e_m^h=||h_m-h_E||_\infty \text{ and } e_m^p=||p_m-p_E||_\infty. \tag{A 17}$$

If the overall spatial accuracy of our numerical approximations is second order, then the ratios e_i^l/e_{i+1}^l should approach 2. Table 4 verifies the second-order spatial accuracy for this linear model problem.

Moving to the nonlinear tear film system with a forcing term such that the true solutions (A 13) and (A 14) satisfy the problem, we find that if $S=10^{-2}$, then the error continues to grow throughout the simulation and contaminates the discrete solution. However, when $S=10^{-3}$, the maximum absolute error shown in table 5 behaves similar to the linear model problem.

Finally, we test the eye-shaped composite grid shown in figure 3. Using the true solutions (A 13) and (A 14), we integrate the forced nonlinear tear film system to $t=1$ with $S=10^{-5}$. The maximum absolute errors are $e^h=5.19\times 10^{-3}$ and $e^p=9.30\times 10^{-4}$.

	e_1^l	e_2^l	e_3^l	e_1^l/e_2^l	e_2^l/e_3^l
$l=h$	0.223	0.115	0.054	1.940	2.130
$l=p$	0.017	0.007	0.004	2.429	1.75

TABLE 5. Maximum absolute error for nonlinear tear film problem of h and p at $t=1$ with $S=10^{-3}$.

REFERENCES

BECKER, J. & GRÜN, G. 2005 The thin-film equation: recent advances and some new perspectives. *J. Phys. Condens. Matter* **17** (9), S291–S307.

BECKER, J., GRÜN, G., SEEMANN, R., MANTZ, H., JACOBS, K., MECKE, K. R. & BLOSSEY, R. 2002 Complex dewetting scenarios captured by thin film models. *Nature Materials* **2**, 59–63.

BERGER, R. E. & CORRSIN, S. 1974 A surface tension gradient mechanism for driving the precorneal tear film after a blink. *J. Biomech.* **7**, 225–238.

BERTOZZI, A. L., BRENNER, M. P., DUPONT, T. F. & KADANOFF, L. P. 1994 Singularities and similarities in interface flows. In *Trends and Perspectives in Applied Mathematics* (ed. L. Sirovich), pp. 155–208. Springer.

BRAUN, R. J. & FITT, A. D. 2003 Modelling drainage of the precorneal tear film after a blink. *Math. Med. Biol.* **20**, 1–28.

BRAUN, R. J. & KING-SMITH, P. E. 2007 Model problems for the tear film in a blink cycle: single equation models. *J. Fluid Mech.* **586**, 465–490.

BRAUN, R. J., USHA, R., MCFADDEN, G. B., DRISCOLL, T. A., COOK, L. P. & KING-SMITH, P. E. 2009 Thin film dynamics on a prolate spheroid with application to the cornea. (submitted).

BRENAN, K. E., CAMPBELL, S. L. & PETZOLD, L. R. 1989 *Numerical Solution of Initial-Value Problems in Differential-Algebraic Equations*. Elsevier.

BRON, A. J., TIFFANY, J. M., GOUVEIA, S. M., YOKOI, N. & VOON, L. W. 2004 Functional aspects of the tear film lipid layer. *Exp. Eye Res.* **78**, 347–388.

CHESSHIRE, G. & HENSHAW, W. 1990 Composite overlapping meshes for the solution of partial differential equations. *J. Comput. Phys.* **90**, 1–64.

CREECH, J. L., DO, L. T., FATT, I. & RADKE, C. J. 1998 In vivo tear-film thickness determination and implications for tear-film stability. *Curr. Eye Res.* **17**, 1058–1066.

DOANE, M. G. 1981 Blinking and the mechanics of the lacrimal drainage system. *Ophthalmology* **88**, 844–851.

FATT, I. & WEISSMAN, B. A. 1992 *Physiology of the Eye: An Introduction to the Vegetative Functions*. Butterworth-Heinemann.

GIPSON, I. K. 2004 Distribution of mucins at the ocular surface. *Exp. Eye Res.* **78**, 379–388.

GOLDING, T. R., BRUCE, A. S. & MAINSTONE, J. C. 1997 Relationship between tear-meniscus parameters and tear-film breakup. *Cornea* **16**, 649–661.

GORLA, M. S. R. & GORLA, R. S. R. 2004 Rheological effects of tear film rupture. *Intl J. Fluid Mech. Res.* **31**, 552–562.

GREER, J. B., BERTOZZI, A. L. & SAPIRO, G. 2006 Fourth-order partial differential equations on general geometries. *J. Comput. Phys.* **216** (1), 216–246.

GRÜN, G. & RUMPF, M. 2000 Nonnegativity preserving convergent schemes or the thin film equations. *Numer. Math.* **87**, 113–152.

HARRISON, W. W., BEGLEY, C. G., LUI, H., CHEN, M., GARCIA, M. & SMITH, J. A. 2008 Menisci and fullness of the blink in dry eye. *Optom. Vis. Sci.* **85**, 706–714.

HENSHAW, W. D. 2002 OGEN: the overture overlapping grid generator. *Tech. Rep.* UCRL-MA-132237. Lawrence Livermore National Laboratory.

HERYUDONO, A., BRAUN, R. J., DRISCOLL, T. A., MAKI, K. L., COOK, L. P. & KING-SMITH, P. E. 2007 Single-equation models for the tear film in a blink cycle: realistic lid motion. *Math. Med. Biol.* **24** (4), 347–377.

JOHNSON, M. E. & MURPHY, P. J. 2004 Changes in the tear film and ocular surface from dry eye syndrome. *Progr. Ret. Eye Res.* **23**, 449–474.

Johnson, M. E. & Murphy, P. J. 2006 Temporal changes in the tear menisci following a blink. *Exp. Eye Res.* **83**, 517–525.

Jones, M. B., McElwain, D. L. S., Fulford, G. R., Collins, M. J. & Roberts, A. P. 2006 The effect of the lipid layer on tear film behaviour. *Bull. Math. Biol.* **68**, 1355–1381.

Jones, M. B., Please, C. P., McElwain, D. S., Fulford, G. R., Roberts, A. P. & Collins, M. J. 2005 Dynamics of tear film deposition and drainage. *Math. Med. Biol.* **22**, 265–288.

Jossic, L., Lefevre, P., de Loubens, C., Magnin, A. & Corre, C. 2009 The fluid mechanics of shear-thinning tear substitutes. *J. Non-Newtonian Fluid Mech.* **61**, 1–9.

King-Smith, P. E., Fink, B. A., Hill, R. M., Koelling, K. W. & Tiffany, J. M. 2004 The thickness of the tear film. *Curr. Eye Res.* **29**, 357–368.

King-Smith, P. E., Fink, B. A., Nichols, K. K., Hill, R. M. & Wilson, G. S. 2000 The thickness of the human precorneal tear film: evidence from reflection spectra. *Invest. Ophthalmol. Vis. Sci.* **40**, 3348–3359.

Kondic, L. & Diez, J. 2001 Pattern formation in the flow of thin films down an incline: constant flux configuration. *Phys. Fluids* **13** (11), 3168–3184.

Lee, Y. C., Thompson, H. M. & Gaskell, P. H. 2007 An efficient adaptive multigrid algorithm for predicting thin film flow on surfaces containing localized topographic features. *Comp. Fluids* **36**, 838–855.

Lemp, M. A. 2007 The definition and classification of dry eye disease: report of the definition and classification subcommittee of the international dry eye workshop. *Ocul. Surf.* **5**, 75–92.

Maki, K. L. 2009 Computational solution of linear systems and models for the human tear film. PhD thesis, University of Delaware.

Maki, K. L., Braun, R. J., Driscoll, T. A. & King-Smith, P. E. 2008 An overset grid method for the study of reflex tearing. *Math. Med. Biol.* **25**, 187–214.

Maki, K. L., Braun, R. J., Henshaw, W. D. & King-Smith, P. E. 2010 Tear film dynamics on an eye-shaped domain. Part I. Pressure boundary conditions. *Math. Med. Biol.* (in press).

Mathers, W. D. & Daley, T. E. 1996 Tear flow and evaporation in patients with and without dry eye. *Ophthalmology* **103**, 664–669.

Maurice, D. M. 1973 The dynamics and drainage of tears. *Intl Ophthalmol. Clin.* **13**, 103–116.

Miljanović, B., Dana, R., Sullivan, D. A. & Schaumberg, D. A. 2007 Impact of dry eye syndrome on vision-related quality of life. *Am. J. Ophthalmol.* **143**, 409–415.

Miller, D. 1969 Measurement of the surface tension of tears. *Arch. Ophthalmol.* **82**, 368–371.

Mishima, S. 1965 Some physiological aspects of the precorneal tear film. *Arch. Ophthalmol.* **73**, 233–241.

Mishima, S., Gasset, A., Klyce, S. D. & Baum, J. L. 1966 Determination of tear volume and tear flow. *Ophthalmol. Vis. Sci.* **5**, 264–276.

Nagyová, B. & Tiffany, J. M. 1999 Components responsible for the surface tension of human tears. *Curr. Eye Res.* **19**, 4–11.

Naire, S., Braun, R. J. & Snow, S. A. 2000 Limiting cases of gravitational drainage of a vertical free film for evaluating surfactants. *SIAM J. Appl. Math.* **61**, 889–913.

Oron, A. & Bankoff, S. G. 2001 Dynamics of a condensing liquid film under conjoining/disjoining pressures. *Phys. Fluids* **13** (5), 1107–1117.

Owens, H. & Phillips, J. 2001 Spread of the tears after a blink: velocity and stabilization time in healthy eyes. *Cornea* **20**, 484–487.

Piegl, L. A. & Tiller, W. 1997 *The NURBS Book*. Springer.

Read, S. A., Collins, M. J., Carney, L. G. & Franklin, R. J. 2006 The topography of the central and peripheral cornea. *Invest. Ophthalmol. Vis. Sci.* **47**, 1404–1415.

Schein, O. D., Munoz, B., Tielsvh, J. M., Bandeen-Roche, K. & West, S. 1997 Prevalence of dry eye among the elderly. *Am. J. Ophthalmol.* **124**, 723–728.

Schwartz, L. W., Roy, R. V., Eley, R. E. & Petrash, S. 2001 Dewetting patterns in a drying liquid film. *J. Coll. Interface Sci.* **234**, 363–374.

Sharma, A., Tiwari, S., Khanna, R. & Tiffany, J. M. 1998 Hydrodynamics of meniscus-induced thinning of the tear film. In *Lacrimal Gland, Tear Film, and Dry Eye Syndromes 2* (ed. D. A. Sullivan, D. A. Dartt & M. A. Meneray), pp. 425–431. Plenum.

Tiffany, J. M. 1991 The viscosity of human tears. *Intl Ophthalmol.* **15**, 371–376.

TIFFANY, J. M., TODD, B. S. & BAKER, M. R. 1998 Computer-assisted calculation of exposed area of the human eye. In *Lacrimal Gland, Tear Film, and Dry Eye Syndromes 2* (ed. D. A. Sullivan, D. A. Dartt & M. A. Meneray), pp. 433–439. Plenum.

WANG, J., FONN, D., SIMPSON, T. L. & JONES, L. 2003 Precorneal and pre- and postlens tear film thickness measured indirectly with optical coherence tomography. *Invest. Ophthalmol. Vis. Sci.* **44**, 2524–2528.

WARNER, M. R. E., CRASTER, R. V. & MATAR, O. K. 2002 Dewetting of ultrathin surfactant-covered films. *Phys. Fluids* **14** (11), 4040–4054.

WITELSKI, T. P. & BOWEN, M. 2003 ADI schemes for higher-order nonlinear diffusion equations. *Appl. Numer. Math.* **45** (2–3), 331–351.

WONG, H., FATT, I. & RADKE, C. J. 1996 Deposition and thinning of the human tear film. *J. Coll. Interface Sci.* **184**, 44–51.

ZHORNITSKAYA, L. & BERTOZZI, A. L. 2000 Positivity-preserving numerical schemes for lubrication-type equations. *SIAM J. Numer. Anal.* **37** (2), 523–555.

ZHU, H. & CHAUHAN, A. 2005 A mathematical model for tear drainage through the canaliculi. *Curr. Eye Res.* **30**, 621–630.